

Testbeam analysis of biasing structures for irradiated hybrid pixel detectors

A. G. Rennie^{a,1,2} C. M. Buttar^b Y. Gao^c R. González López^d D. Maneuski^b E. Pender^c
Q. Qin^e M. Sullivan^d J. T. Taylor^d K. Wraight^b

^aUniversity of California, Irvine

Department of Physics and Astronomy, 4129 Frederick Reines Hall, Irvine, CA 92697-4575

^bUniversity of Glasgow

School of Physics and Astronomy, Kelvin Building, University Avenue, Glasgow, G12 8QQ

^cUniversity of Edinburgh

School of Physics and Astronomy, James Clerk Maxwell Building, Peter Guthrie Tait Road, Edinburgh, EH9 3FD

^dUniversity of Liverpool

Department of Physics, Oliver Lodge, Oxford Street, Liverpool, L69 7ZE

^eUniversity of Manchester

Department of Physics and Astronomy, Schuster Building, Oxford Road, Manchester, M13 9PL

E-mail: adam.rennie@cern.ch

ABSTRACT: Following the Phase-II upgrade during Long Shutdown (LS3), the LHC aims to reach a peak instantaneous luminosity of $7.5 \times 10^{34} \text{ cm}^{-2} \text{ s}^{-1}$, which corresponds to an average of around 200 inelastic proton-proton collisions per beam-crossing (every 25 ns). To cope with these conditions, the ATLAS Inner Detector will be replaced by a new all-silicon system — the Inner Tracker (ITk). The ITk will be operational for more than ten years, during which time ATLAS is expected to record approximately 4000 fb^{-1} of data. The ITk's pixel sub-system is based on hybrid pixel modules with new silicon sensors and readout chips. These studies focus on testbeam campaigns undertaken to study the spatial resolution and efficiencies of hybrid pixel detector modules based on the first large-structure prototype front-end readout chip — the RD53A — using planar silicon sensors. These devices have been irradiated to replicate the effect of the high radiation environment present during operation in the ATLAS detector. Results for devices using sensors with different punch-through bias structures and using different readout modes are summarised. Those with sensors incorporating a punch-through bias structure are found to exhibit systematically lower efficiency than those without, as a result of local areas of relative inefficiency around the punch-through dots. Despite this, all devices measured are found to satisfy the requirement of 97% efficiency at $V_{\text{bias}} = 400 \text{ V}$ after being irradiated to end-of-life fluence.

KEYWORDS: Hybrid detectors, Radiation-hard detectors, Particle tracking detectors (Solid-state detectors), Performance of High Energy Physics Detectors

¹Corresponding author.

²Previously at University of Glasgow, School of Physics and Astronomy, Kelvin Building, University Avenue, Glasgow, G12 8QQ.

Contents

1	Introduction	2
2	Devices under test	2
3	Testbeam facilities and detector setup	4
4	Reconstruction and analysis	6
4.1	Reconstruction: EU Telescope	7
4.2	Analysis: TBmon2	10
5	Results	12
5.1	October 2018 testbeam	12
5.2	December 2018 testbeam	15
5.3	Cross-testbeam comparisons	20
6	Conclusions	20

1 Introduction

For the High Luminosity era of the Large Hadron Collider (HL-LHC), the present ATLAS Inner Detector will be replaced by a new all-silicon Inner Tracker (ITk) [1, 2] in order to cope with increased occupancy and radiation. The ITk will consist of a pixel detector closest to the beamline and a strip detector for the outer section. This will provide coverage for charged particle reconstruction up to $|\eta| < 4$. The ATLAS upgrade physics programme drives the design and performance requirements of the pixel detector. The demand for high precision, radiation hard, rapid readout pixel modules has required the design of a new front-end readout chip and sensor architecture to meet the performance requirements necessary for the HL-LHC environment.

The pixel detector will consist of five barrel layers in the central region, and a number of ring-shaped layers in the forward region, leading to a total active area of around 13 m^2 . The innermost two layers of the ITk pixel detector [3] — the *inner system* — will experience the highest total ionising dose and so will feature 3D silicon sensors, which have heightened radiation hardness. The inner system is designed to be replaced after 2000 fb^{-1} . All remaining layers — the *outer system* — will be based on planar silicon sensors with thickness $150 \mu\text{m}$. Novel front-end ASICs, implemented in 65 nm technology, are connected to the silicon sensors using bump-bonding to form a bare modules. This is then glued and wire-bonded to a flexible printed circuit board (PCB). The off-detector readout electronics will be implemented in the framework of the general ATLAS trigger and DAQ system with a readout rate of up to 5 Gb/s per data link for the innermost layers.

The outer system is expected to experience a fluence up to $5 \times 10^{15} n_{\text{eq}} \text{ cm}^{-2}$ and a total ionising dose of 5 MGy .

Testbeam measurements are vital to study, understand, and verify the performance of the new readout chips and sensor technologies. This paper summarises several testbeam campaigns undertaken for several R&D sensors developed by the ATLAS UK ITk community. Different biasing structures, readout modes, and pixel module operation parameters such as the bias voltage and threshold are studied in detail using irradiated devices in order to mimic the effects of LHC operation on the detector modules.

2 Devices under test

The devices under test (DUTs) are hybrid pixel modules, each including a passive high resistivity silicon sensor (*n-in-p*) and a front-end readout chip combined by flip-chip bump-bonding, and a flexible PCB. In this paper, prototype modules with different silicon sensor designs, together with a prototype front-end readout chip, the RD53A [4], are characterised. The sensors were manufactured by Micron Semiconductor Ltd.

The DUTs presented here were all irradiated at the Karlsruher Institut für Technologie (KIT) to $3.4 \times 10^{15} n_{\text{eq}} \text{ cm}^{-2}$ using 25 MeV protons extracted from the Karlsruhe Kompakt Zyklotron [5]. This fluence is based on the expected radiation levels in the outer system of the ATLAS pixel detector.

Devices made from two different planar silicon *n-in-p* sensors are presented. Both sensors have the same pixel pitch ($50 \times 50 \mu\text{m}^2$) and thickness ($150 \mu\text{m}$), but are differentiated by *punch-through bias* (PTB) structure. Once in operation, the PTB structure is inactive. However, it serves

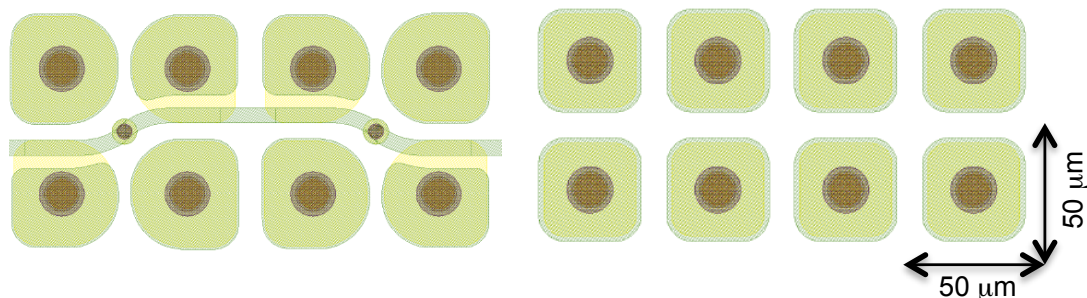


Figure 1: Pixel sensor designs with (left) and without (right) biasing structures [6]. The design with biasing structure implemented uses punch-through dots common to four pixel cells, connected to a biasing rail in a zigzag configuration.

a vital role in the production of the pixel modules in allowing for electrical testing of the sensor ahead of bump-bonding. Being able to measure the sensor IV curve before assembling a complete module can help keep the final module yields at higher levels than if this testing is restricted to fully assembled modules. Although beneficial in production, the PTB structure can also reduce charge collection efficiency of the sensor. The small depletion region around the punchthrough dots in the sensor captures some charge, resulting in a reduction of the hit efficiency in the region around the dot. In spite of this, the removal of these biasing structures is heavily disfavoured. In the measurements presented here, one device — referred to as DUT-A — has no PTB structure, whilst the other device — referred to as DUT-B — has a zigzag PTB structure variation, expected to reduce the loss of charge collection. These structures are shown in Figure 1.

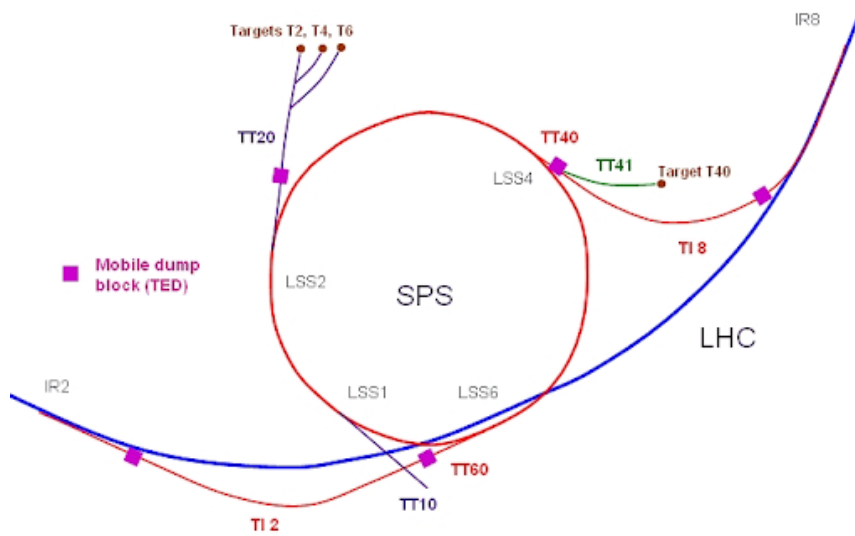
The final production front-end chip for the ITk pixel system — the ITkPix — will have 400×384 pixels over an area of $20.1 \times 21.6 \text{ mm}^2$. This will provide the resolution required throughout the ITk for precision track reconstruction. The ASIC will be a radiation hard CMOS chip with output data compression for the high radiation dose and data output requirements of the inner detector.

For the R&D phase, a first large-scale prototype chip, the RD53A [4], was produced in 65 nm CMOS technology by TSMC. RD53A is the basis for production designs for the ATLAS and CMS pixel detector upgrades for the HL-LHC era. The RD53A chip contains 400×192 pixels over an area of $20.1 \times 11.6 \text{ mm}^2$, half the area of the ITkPix. The RD53A chip has been designed to meet the radiation tolerance of 5 MGy, thinned to 150 μm.

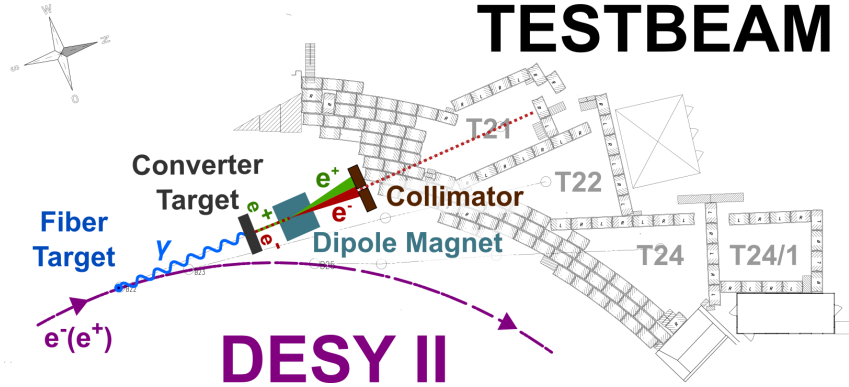
Three different analogue front-ends — *linear*, *differential* and *synchronous* — have been designed and implemented in the chip. The linear front-end uses a linear pulse amplification in front of the discriminator, comparing the pulse to some threshold voltage. The differential front-end uses a differential gain stage in front of the discriminator. It then implements a threshold by unbalancing the two branches. Finally, the synchronous front-end uses a baseline “auto-zeroing” scheme. Rather than pixel-by-pixel threshold trimming, this requires the periodic acquisition of a baseline. Detailed evaluation programmes have been carried out in both ATLAS and CMS experiments for all three front-ends to select the most suitable design for their respective operation requirements. The devices used in these tests incorporate split the chip into three regions covering equal areas on the sensor, corresponding to the three readout modes.

3 Testbeam facilities and detector setup

Testbeam facilities The testbeam campaigns considered in this paper were carried out at two facilities: the SPS testbeam facility at CERN and the DESY testbeam facility in Hamburg. The CERN SPS testbeam facility, shown in Figure 2a, is built around the SPS beamline [7] and supplies a beam of 120 GeV pions from converted protons. The DESY testbeam facility, shown in Figure 2b, is built around DESY-II electron-positron synchrotron and supplies a beam of 1–6 GeV electrons from converted bremsstrahlung radiation. Both testbeam facilities house an EUDET-type [8] telescope providing identical apparatus at both sites, facilitating equivalent data reconstruction and analysis. Data was taken using the BDAQ readout system [9].



(a) Schematic of the CERN SPS testbeam facility [7].



(b) Schematic of the DESY testbeam facility [10].

Figure 2: Testbeam facilities used to make measurements of device efficiency.

The difference between the two sites comes from the beam supplied. The nature of the beam must be considered in the analysis due to the effect of multiple scattering, which occurs due to the Coulomb forces between the atoms in the detector material and the charged particles in the beam. This effect is larger at lower beam-momentum and contributes to the uncertainty on the track

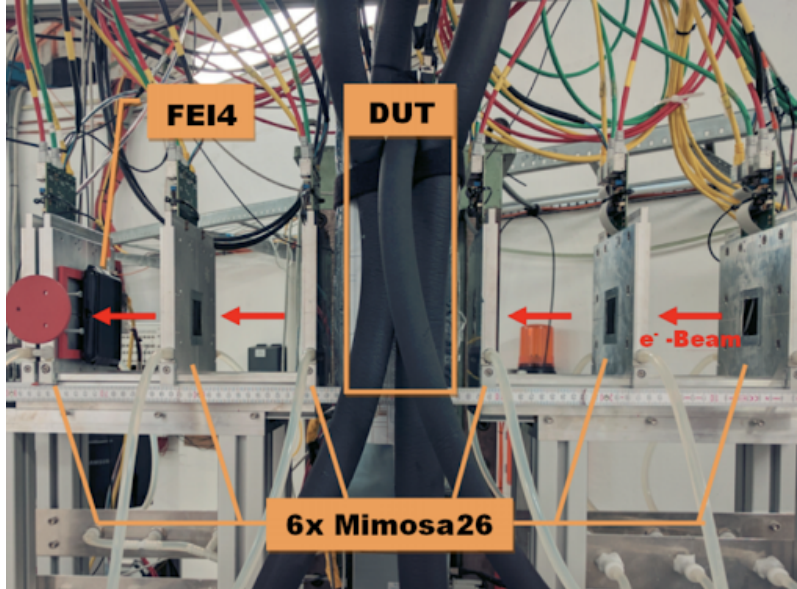


Figure 3: Telescope configuration at a DESY testbeam campaign. The DUT is placed between three upstream and three downstream MIMOSA-26 devices with high spatial resolution. Timing information is provided by an FE-I4 device fixed at the end of the telescope.

resolution.

Telescope setup An EUDET-type beam telescope, with a setup equivalent to that shown in Figure 3, is used to measure the track of a charged beam through the DUT.

The telescope contains six MIMOSA-26 [11] devices which are based on monolithic active pixel sensor technology with binary readout. These pixel modules have high spatial resolution which translates into a high resolution on reconstructed tracks. Each device covers an area of $21.5 \times 13.7 \text{ mm}^2$ and has 576×1152 pixels with a pitch of $18.4 \times 18.4 \mu\text{m}^2$ and a thickness of $50 \mu\text{m}$, reducing the effect of multiple scattering. The MIMOSA-26 devices are operated in rolling shutter readout mode with an integration time of around $115.2 \mu\text{s}$. This corresponds to a readout rate of around 8 kHz, much slower than the 40 MHz DUT readout rate [12]. This means that for a given event read from a DUT, corresponding to a single trigger, there may be several tracks reconstructed in the telescope planes, corresponding to several triggers. Removing these out-of-time contributions from the analysis is essential to measuring the DUT efficiency. For this reason, an additional timing reference plane is placed at the end of the telescope. This timing plane is an FE-I4 pixel module [13], with the same readout rate as the DUT. This FE-I4 module has pixels with pitch of $50 \times 250 \mu\text{m}^2$. Reconstructed tracks to be used for the analysis of the DUT are then required to have an associated hit in the timing plane.

Data acquisition The telescope uses dedicated trigger hardware called the trigger logic unit (TLU). The TLU receives a signal from two scintillators placed either side of the telescope and generates triggers which it distributes to the DUT, telescope planes, and timing reference. Each trigger is uniquely timestamped, within a resolution of 1.5 ns [14], enabling the synchronisation of hits across all planes. In addition, the DUT may respond to the TLU to indicate that it is busy, ensuring that no

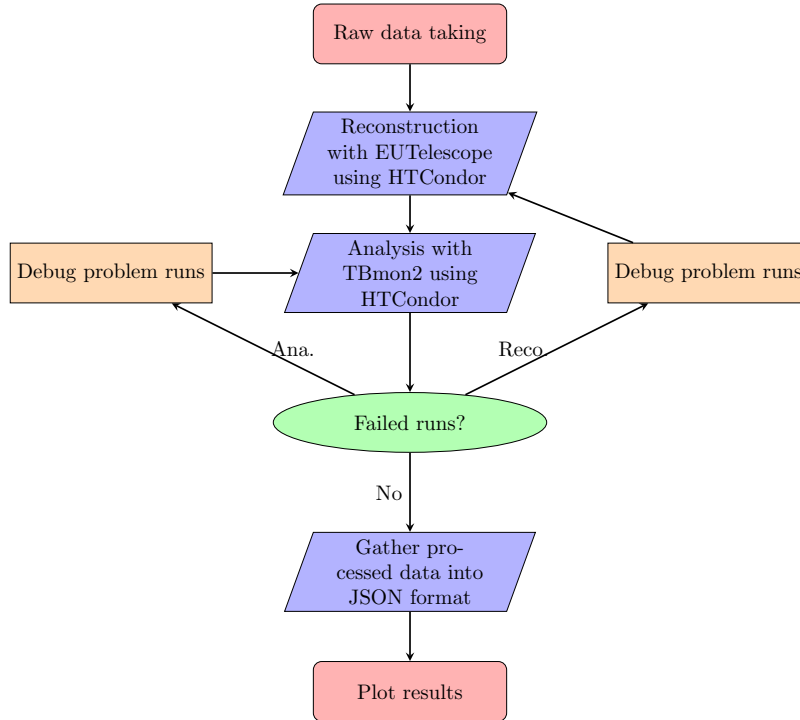


Figure 4: Flowchart showing the workflow for the results presented here, from the raw data-taking to final analysis of the reconstructed data.

trigger signal is lost during the integration time. The EUDAQ software, used in conjunction with the the TLU, merges individual data streams into one and saves in histogram format for reconstruction.

Testbeam campaigns Data was taken in October 2018 and December 2018 at the CERN SPS and DESY facilities, respectively. Table 1 lists the testbeam campaigns and DUTs present for each.

Table 1: DUT and operating parameters for each testbeam campaign.

<i>Campaign</i>	<i>Beam</i>	<i>DUT (FE)</i>	<i>PTB</i>	<i>Bias voltage (V)</i>	<i>Threshold (e⁻)</i>
CERN Oct. 2018	120 GeV pions	DUT-A (lin)	none	600	1200, 1600
		DUT-A (diff)		600	1160, 1680, 2140
DESY Dec. 2018	1–6 GeV electrons	DUT-A (lin)	none	200, 400, 600	1027, 1200
		DUT-B (lin)	zigzag	100, 200, 300, 400, 500, 600	870, 1010, 1120

4 Reconstruction and analysis

The workflow for the results presented here is summarised in Figure 4. The description of each stage in that workflow is given below.

4.1 Reconstruction: EUTelescope

Reconstruction of the testbeam data was carried out using EUTelescope [15], a modular framework widely used for particle trajectory reconstruction in data recorded with beam telescopes. The framework converts the raw data, as registered by the DAQ system, into a standardised data format — LCIO (Linear Collider Input/Output [16]) — with which clusters of hit pixels can be built and assigned to particle tracks.

EUTelescope uses the GEAR (GEometry API for Reconstruction [17]) framework for the geometric description of the framework. The testbeam setup (positions, alignment, detector geometry, sensor layout, etc.) is described by an XML file which is read by the analysis framework to allow for transformations of hit positions from a local frame of reference to the telescope (global) reference frame.

Data conversion and noisy pixel detection The data recorded by the testbeam DAQ system needs to be converted from its original custom format into the standard LCIO format using EUDAQ [18]. LCIO data is event-based, containing an arbitrary amount of collections per triggered event. These collections can contain (hit) pixel indices, clustered pixels, and derived hits as the analysis moves along the reconstruction workflow.

Once the raw data has been converted into the LCIO format, one of EUTelescope processors, EUTelNoisyPixelFinder, can be applied. This uses the firing frequency (occupancy) of the pixels to determine whether a given pixel should be labelled as noisy. Pixels with firing frequency exceeding 0.1% in the case of DUTs and FE-I4 reference, and 0.5% in the case of the MIMOSA-26 planes are identified and removed from subsequent data analysis.

Clustering Neighbouring hit pixels belonging to the same LCIO collection are grouped and stored in a new cluster collection. Taking the masks created in the previous step, clusters containing at least one noisy pixel are tagged as noisy. Figure 5 shows typical distributions of total cluster charge in the form of time over threshold (ToT). The cluster charge is the sum of the charges of hit pixels forming the cluster. Also shown in the figure is the cluster size — the number of hit pixels forming a cluster.

Hitmaker and pre-alignment Using the cluster collections obtained in the previous step, hit positions in the local frame of reference are defined as the centre of the cluster coordinate, calculated as the charge-weighted centre of the position of the hits forming the cluster:

$$\bar{x} = \frac{1}{Q} \sum_{i=0}^N x_i q_i, \quad (4.1)$$

where x_i is the position of the i^{th} pixel in the cluster, q_i the charge in that pixel (ToT), and Q the sum of all charges collected by all pixels in the cluster. The position is calculated in the x and y axes independently and stored in a new LCIO collection.

The hit positions are translated from the local frame of reference for each plane to a global frame by rotating and shifting the local coordinates by the angles and global positions registered when performing data-taking (i.e. rotation and position of each plane and DUT in the testbeam). These values are provided by the GEAR file. Once the hits are provided in a global frame of reference,

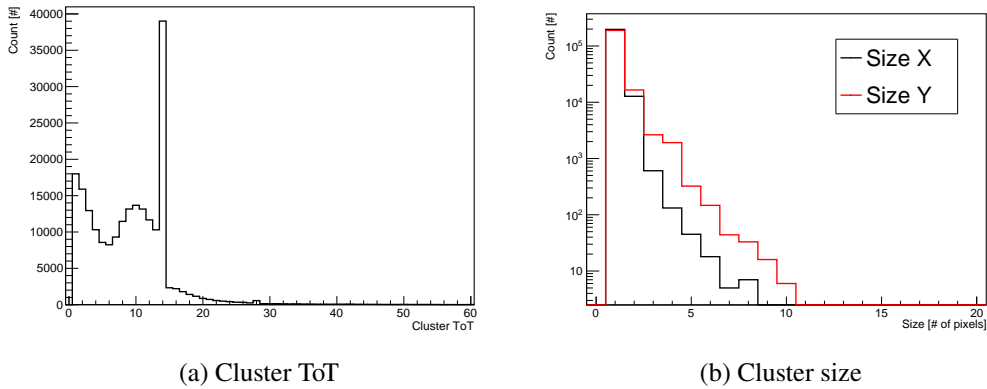
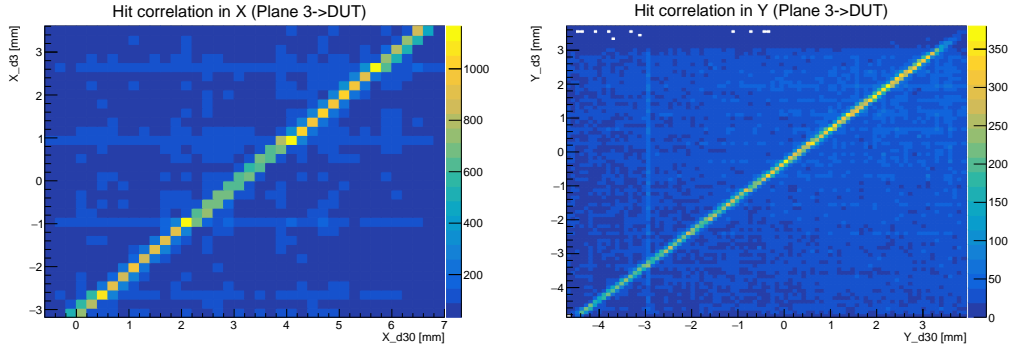


Figure 5: Example run taken during DESY December 2018 testbeam with device DUT-B, $V_{\text{bias}} = 600 \text{ V}$, and FE threshold of 1000 e^- ; (a) Cluster ToT in units of the beam crossing (25 ns). The exponential fall at low ToT originates from background noise. The gaussian-like peak around bin 10 represents the signal. The spike at bin 15 corresponds to noise from broken channels which send a saturated value which translates to 15 [4]. These are removed later in the reconstruction. (b) Cluster size in number of pixels. The vast majority of clusters have a size of 1 pixel.

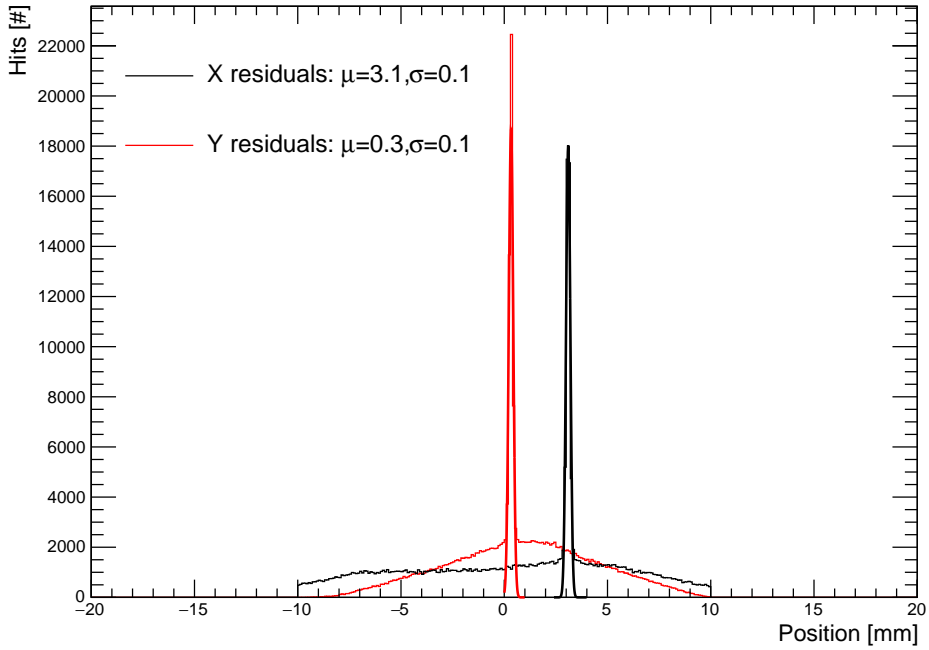
the positions of those hits registered in the first sensor are propagated to all sensors, calculating the difference between the propagated value and the registered hit in each sensor, referred to as residuals. These residuals are registered in one and two-dimensional histograms, taking the bins with highest counts as the pre-alignment factors, representing a rough estimate of the shift of the planes in x and y direction. These pre-alignment values are then written to a new GEAR file to be used in subsequent steps. Examples of correlations of the hit positions in x and y between hits in the DUT and a beam telescope plane are shown in Figure 6, where (c) shows the single dimension projection of (a) and (b) overlaid. The distance of the peak of each projection from the origin represents the displacement of the DUT from its optimum position relative to the telescope planes. This value is used to align plains.

Alignment In this step, updated global hits based on the corrected pre-aligned GEAR file are used to determine precise alignment of the telescope and DUT planes, using track finding and aligning algorithms based on General Broken Lines (GBL) track model [19]. In this model, the beam telescope, consisting of six planes, is divided into two groups – the upstream and downstream triplets. Within each triplet, a straight line (doublet) is calculated joining the first and last hits. Doublets that have slopes inconsistent with the beam direction are excluded to suppress false combinations. The threshold is given by user-defined cuts. The distance between the doublet and the hit in the middle sensor must also be within a user-defined range for the triplet to be considered valid. Both upstream and downstream triplets are then extrapolated to the centre of the beam telescope. The extrapolated position of these two triplets must be matched within a user-defined distance to be joined together as a track. Once the fitted line from each arm of telescope is matched the track is defined.

The alignment process is repeated 3 times per run, using a partial number of events to retrieve and estimate the values of the cuts to be used by GBL. As the alignment process is iterated, cut values



(a) Correlation between hits in the x -direction. (b) Correlation between hits in the y -direction.



(c) Residuals for both x and y directions.

Figure 6: Correlations and residuals between DUT and adjacent telescope plane. The device used in this example has pixel pitch $25 \times 100 \mu\text{m}^2$, visible in the difference in granularity in the two dimensions. Those used in the measurements presented in the following sections all have pitch of $50 \times 50 \mu\text{m}^2$.

are reduced, initially set high for a first estimate of the cut values, then optimised by performing a gaussian fit on the distribution of the distances and slopes previously explained.

Track fitting The final reconstruction step consists of a track fit using the six hits of the telescope planes associated to each track found in the previous step passing all required cuts. The tracks are output to a ROOT n -tuple so that they may be used for subsequent analysis. The resulting residuals for the hits in DUT in x and y , defined as the difference between the reconstructed cluster position and the extrapolated values from the fitted track are shown in Figure 7. Both distributions are

centred around zero, which shows good alignment with no systematic offset. The RMS of each distribution corresponds to the expected resolutions of the pixel pitches in each dimension. The χ^2 per degree of freedom distribution for the track fit peaks at low values and has a smooth tail, implying that the telescope is well aligned over the run.

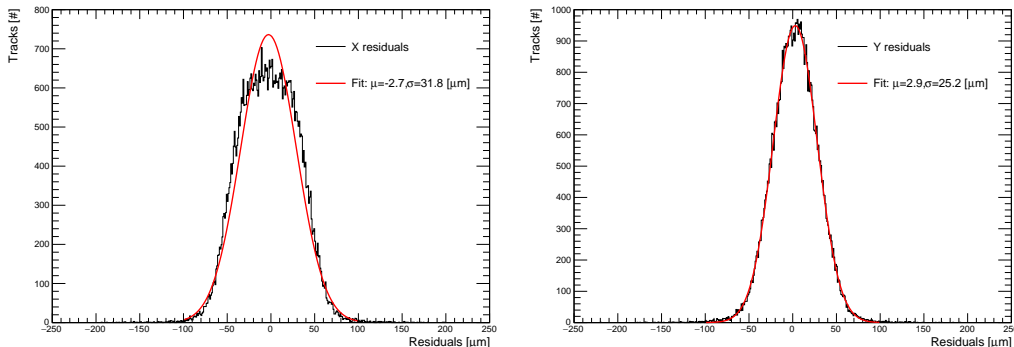


Figure 7: Residual distributions after the track fitting.

4.2 Analysis: TBmon2

The output files produced following reconstruction in EUTelescope are then analysed using TBmon2 [20], a testbeam analysis software package. The framework uses a core processor to read all relevant inputs, such as data paths and DUT geometry files, and then executes data pre-processing and different analyses. These analyses can be individually configured in dedicated configuration files with corresponding DUT specifications. Central configuration parameters, such as selection of fiducial regions and track quality criteria, are set by the user.

The pre-processing module first finds tracks that pass a set of basic quality criteria and are matched to at least one hit in the timing reference plane. When two DUTs with the same readout rate are placed within the telescope planes, it is possible to use either the other RD53A DUT or the FE-I4 as the timing reference plane. To mitigate multiple scattering effect when propagating tracks from the DUT plane to the reference plane, a radius matching requirement is applied on hits from both devices. The maximum distance between hits in each axis in the transverse plane is specified in the configuration file and is commonly set to half of the pitch of the DUT in that direction.

Once the pre-processing is complete, different analysis modules can be executed to study the performance of the DUT. In this paper, we focus on the pixel hit efficiency, defined as the ratio of the number of tracks with matching hits in the DUT to the total number of telescope tracks:

$$\epsilon = \frac{n_{\text{matched tracks}}}{n_{\text{total tracks}}}. \quad (4.2)$$

This quantity is one of the most important figure of merit to qualify sensor designs. During the ATLAS ITk Pixel Sensor Market Survey [3], devices achieving global efficiencies above 98.5% or 97% in the case of unirradiated or irradiated modules, respectively, were considered to have met the production requirements.

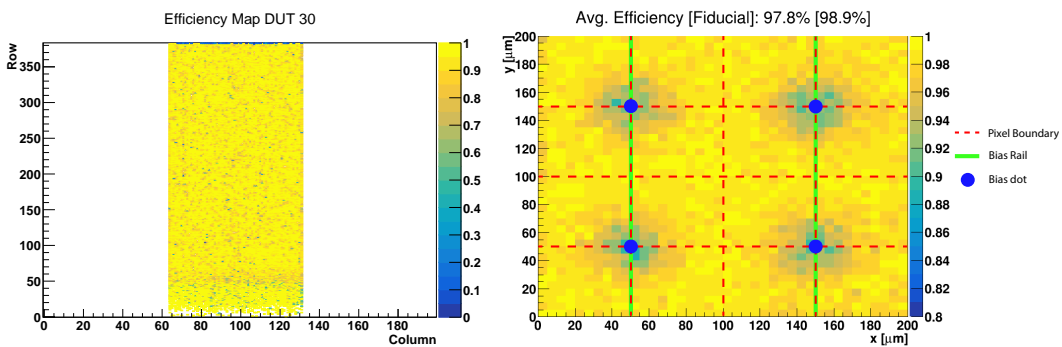
All tracks passing the quality selection criteria applied in the pre-processing are included in the total number of tracks. Hit-to-track matching criteria is specified by maximum matching distance

in the $x - y$ plane between the extrapolated position in the DUT plane from the telescope tracks and the reconstructed pixel hit position in the DUT. The maximum threshold in each axis, x or y , is set to be twice the pitch size in the given axis of the DUT and specified in the configuration file.

In addition to the overall pixel efficiency, more detailed studies are also carried out to characterise the pixel hit efficiency dependence on position within the pixel matrix:

- Pixel hit maps: the efficiency is computed on a pixel-by-pixel basis by considering all hits and tracks which pass through that pixel. The outputs of this analysis are efficiency maps such as that shown in Figure 8a, where the efficiency is only computed for the front-end under study (columns 65-130).
- In-pixel efficiency: this analysis provides an in-depth look at the efficiency patterns that may arise due to different structures present in the device at a sub-pixel level, such as punch-through bias dots. The ability to make such a measurement is only possible as a result of the high resolution of the MIMOSA-26 sensors in the telescope in comparison to the DUTs. In order to analyse the efficiency in such a granular manner, a large number of hits per pixel are required. To achieve this, and avoid the need for extremely long data-taking runs, the full pixel matrix is divided into blocks containing 4×4 pixels each, leading to a total block area of $200 \times 200 \mu\text{m}^2$, with each block across the whole pixel matrix then overlaid on top of one another to provide averaged information from across the whole sensor. The resulting efficiency maps are shown in Figure 8b, where it is possible to distinguish efficiency drops between pixels corresponding to the presence of a punch-through bias dot, which is at the same potential as the charge collection electrode and tends to collect the electrons around it rather than the pixels themselves. A fiducial area can be calculated by masking pixels in the region affected by the punch-through dots, providing a fiducial efficiency as well as the overall efficiency. With reference to Figure 8b, this region is defined in Equation 4.3:

$$(x, y) \in ([0 \mu\text{m}, 20 \mu\text{m}) \cup (80 \mu\text{m}, 120 \mu\text{m}) \cup (180 \mu\text{m}, 200 \mu\text{m})]^2. \quad (4.3)$$



(a) Typical pixel efficiency map using one of (b) Typical in-pixel efficiency map for a device including three front-ends on the RD53A. punch-through bias.

Figure 8: Example run during the December 2018 testbeam campaign (Batch 1, DUT-B, $V_{\text{bias}} = 600 \text{ V}$, threshold = 1000 e^-).

5 Results

Presented in the following sections are results of the final analysis for both testbeam campaigns, as well as a combined set of results comparing devices across campaigns. The criteria later adopted by the ATLAS planar sensor market survey required that devices irradiated to $2 \times 10^{15} n_{\text{eq}} \text{cm}^{-2}$ achieve 97% efficiency at a bias voltage of $V_{\text{bias}} = 400 \text{ V}$ and that devices irradiated to $5 \times 10^{15} n_{\text{eq}} \text{cm}^{-2}$ achieve 97% efficiency at a bias voltage of $V_{\text{bias}} = 600 \text{ V}$. Although these criteria were adopted after the irradiation of the devices measured here, they provide a useful reference point for the expected performance post-irradiation. Where possible, devices are evaluate with reference to the former benchmark and are therefore conservative in that the results presented here are for devices irradiated to $3.4 \times 10^{15} n_{\text{eq}} \text{cm}^{-2}$ — almost double the fluence stipulated for that set of operating parameters. Efficiency values are also evaluated for various other sets of parameters. The statistical uncertainties on the results shown here are too small to be visible on the plots, so are omitted.

5.1 October 2018 testbeam

In this campaign, device DUT-A was characterised using both linear and differential front-ends. It contains no punch-through biasing structure.

Figure 9 shows the overall efficiency as a function of the threshold for the differential and linear FEs, at a $V_{\text{bias}} = 600 \text{ V}$. The highest efficiency of $\varepsilon = 99.47\%$ is observed with a threshold of $1158 e^-$ for the linear FE, and $\varepsilon = 99.05\%$ for the differential FE at a threshold of $1200 e^-$. Increasing the threshold beyond this point, the devices using both of the FEs exhibit a degradation in efficiency. This can be attributed to the loss of signal.

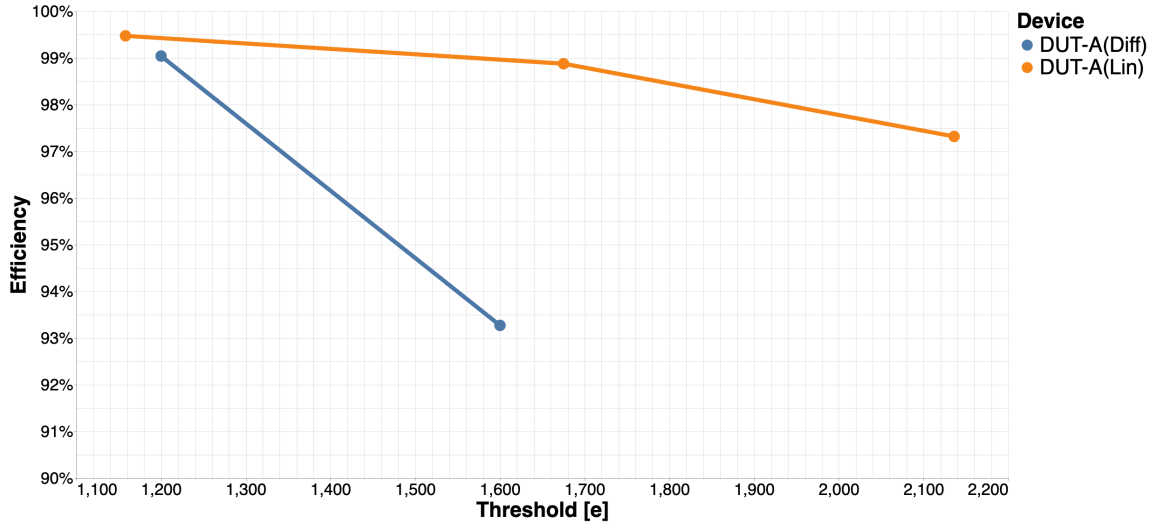


Figure 9: Evolution of the efficiency (as defined in Section 4.1), as a function of threshold, in the October 2018 testbeam for both front-ends at $V_{\text{bias}} = 600 \text{ V}$.

Figure 10 shows the in-pixel efficiency maps for the linear FEs at different thresholds. At the optimum threshold, the efficiency exhibits near-uniform distribution across the sensor. At higher threshold settings, efficiencies are reduced close to the pixel corner boundaries as a result of charge-sharing. Figure 11 shows the in-pixel efficiency maps for the differential FEs at different thresholds.

It can be seen that the device efficiency drops as the threshold is raised beyond the efficiency plateau such that signal is being cut away.

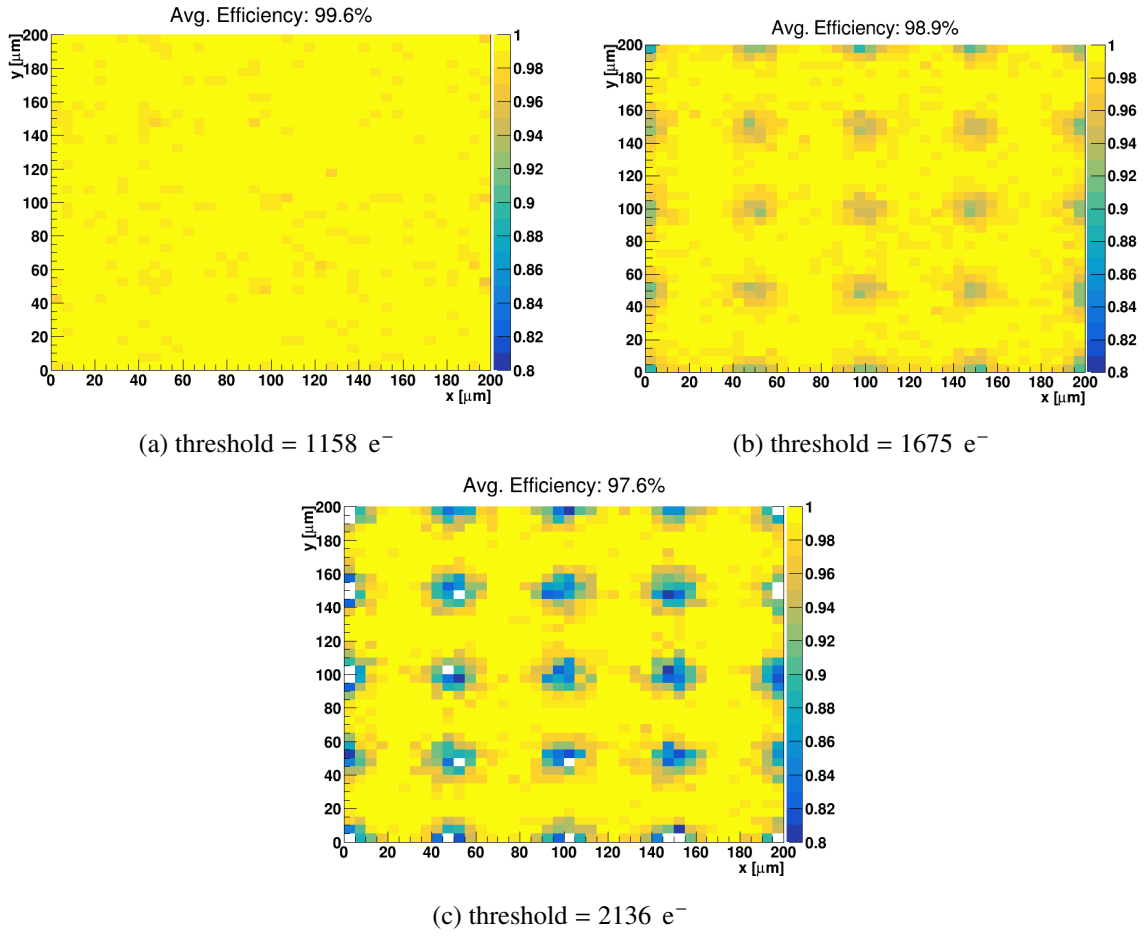


Figure 10: In-pixel efficiency maps, as defined in Section 4.2, for device DUT-A (linear FE) with $V_{\text{bias}} = 600 \text{ V}$.

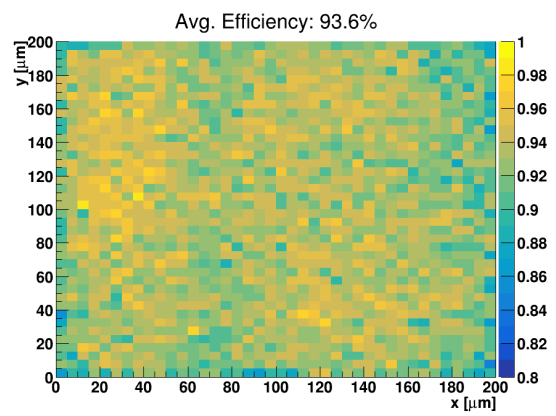
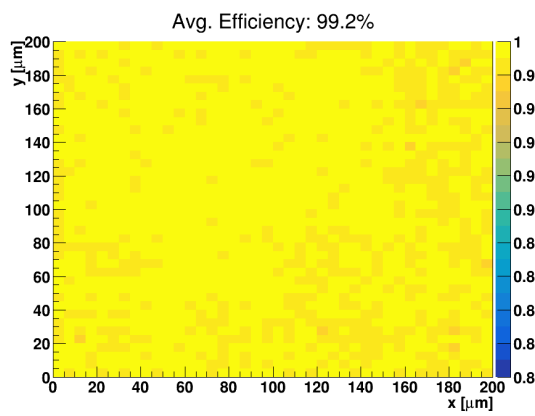


Figure 11: In-pixel efficiency maps for device DUT-A (differential FE) with $V_{\text{bias}} = 600$ V.

5.2 December 2018 testbeam

In this campaign, both devices DUT-A and DUT-B were characterised using the linear front-end. DUT-A contains no PTB structure, whilst DUT-B uses the zigzag PTB structure.

Figure 12 shows the overall efficiency as a function of the V_{bias} for both DUTs. In such comparisons, the efficiency values displayed for DUT-B are the global efficiencies, as opposed to those for the fiducial area previously defined in Equation 4.3. Both devices behave as expected, with efficiency increasing as V_{bias} increases before reaching a plateau. The efficiency reaches plateau by $V_{\text{bias}} = 300$ V and $V_{\text{bias}} = 400$ V for device DUT-B and DUT-A, respectively. Figure 13 shows the overall efficiency as a function of the threshold for both DUTs. The highest efficiency achieved for device DUT-B is observed with threshold = $1013 e^-$ at $V_{\text{bias}} = 600$ V. An efficiency of $\varepsilon = 99.55\%$ is reached for DUT-A at threshold = $1027 e^-$ at $V_{\text{bias}} = 600$ V. At $V_{\text{bias}} = 400$ V, both devices exceed the 97% efficiency criterion. Device DUT-B reaches the desired efficiency when using a threshold above $1000 e^-$. For device DUT-A, the desired efficiency is reached for all threshold points with $V_{\text{bias}} \geq 400$ V.

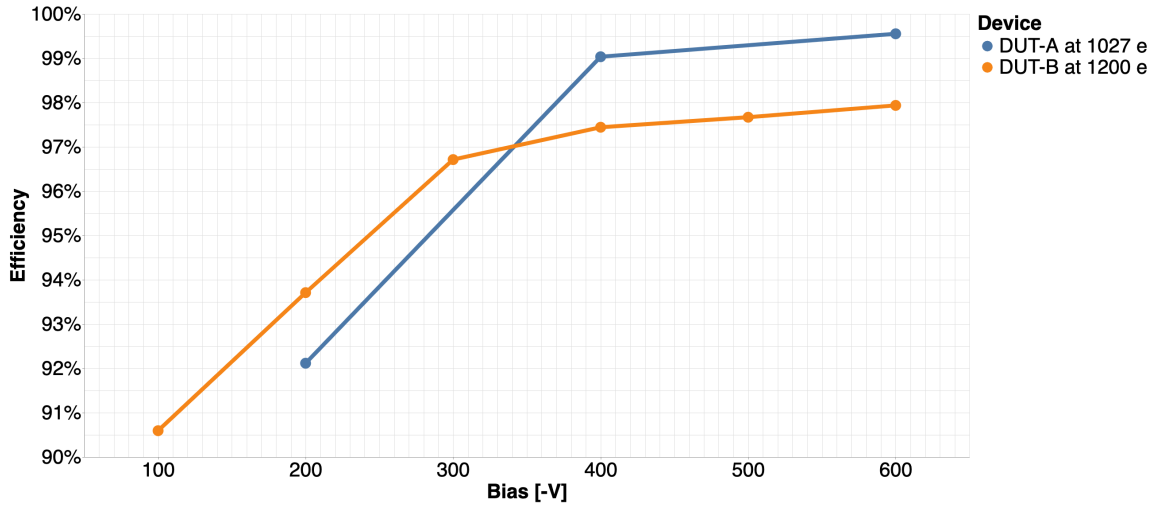


Figure 12: Evolution of the efficiency as a function of bias voltage during the December 2018 testbeam with threshold = $1200 e^-$ (DUT-B) and threshold = $1027 e^-$ (DUT-A). Both devices are using the linear front-end.

Figure 14 shows the in-pixel efficiency maps for device DUT-B at different V_{bias} points, with a threshold of $1200 e^-$. Here, the efficiency of the device increases as V_{bias} is increased. Despite reaching near-perfect efficiency across the majority of the sensor, the regions around the punch-through dots retain their lower efficiency. Figure 15 shows the in-pixel efficiency maps for the same device at different threshold points and $V_{\text{bias}} = 600$ V. Here, the efficiency of the device increases as the threshold is increased, until the efficiency reaches a plateau at the higher threshold values. Beyond this, an increase in the threshold begins to remove signal hits, to the detriment of the device efficiency. As with the V_{bias} scan, the regions around the punch-through dots have a persistently lower efficiency than the other areas on the sensor, which reach near-perfect efficiency. Figure 16 shows the in-pixel efficiency maps for device DUT-A at different V_{bias} points, with a threshold of $1027 e^-$. Here, the efficiency of the device increases as the threshold is increased.

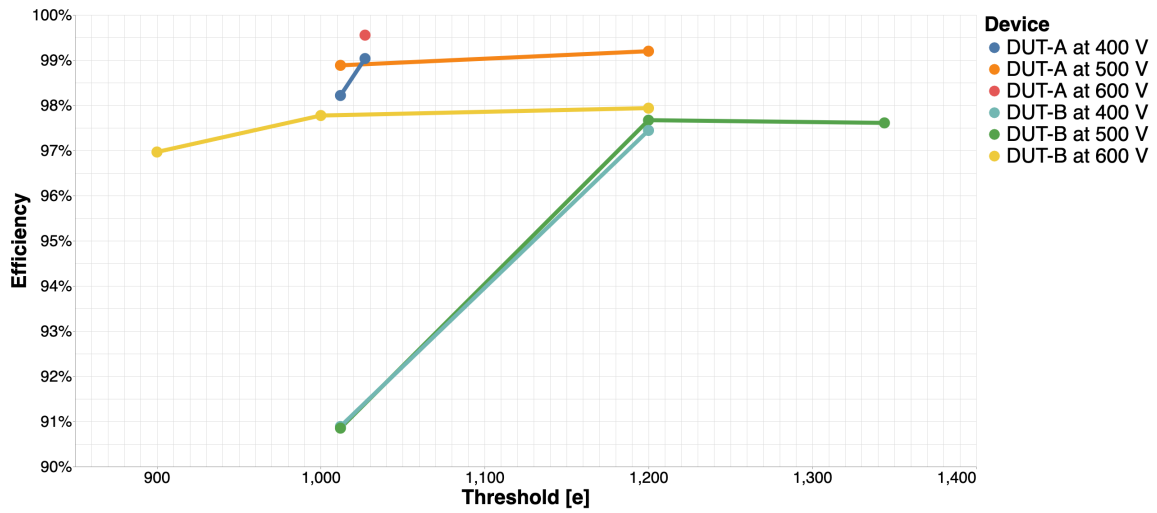


Figure 13: Evolution of the efficiency as a function of threshold during the December 2018 testbeam for both devices, using the linear front-end.

Despite reaching near-perfect efficiency across the majority of the sensor at higher threshold values, the regions around the pixel corners exhibit lower efficiency at lower threshold as a result of charge-sharing.

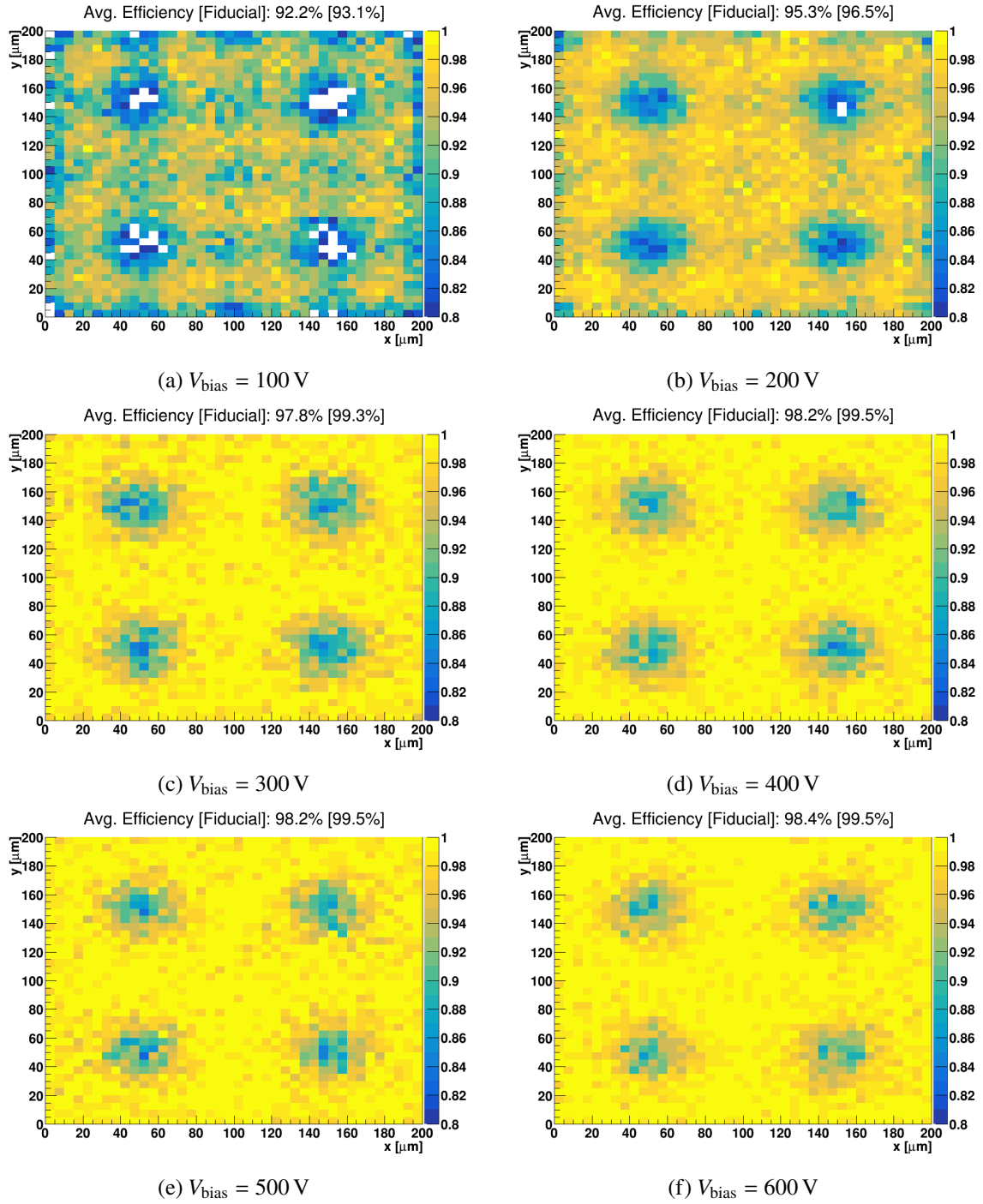


Figure 14: In-pixel efficiency maps, as defined in Section 4.2, for device DUT-B (linear FE) with a threshold of 1200 e^- .

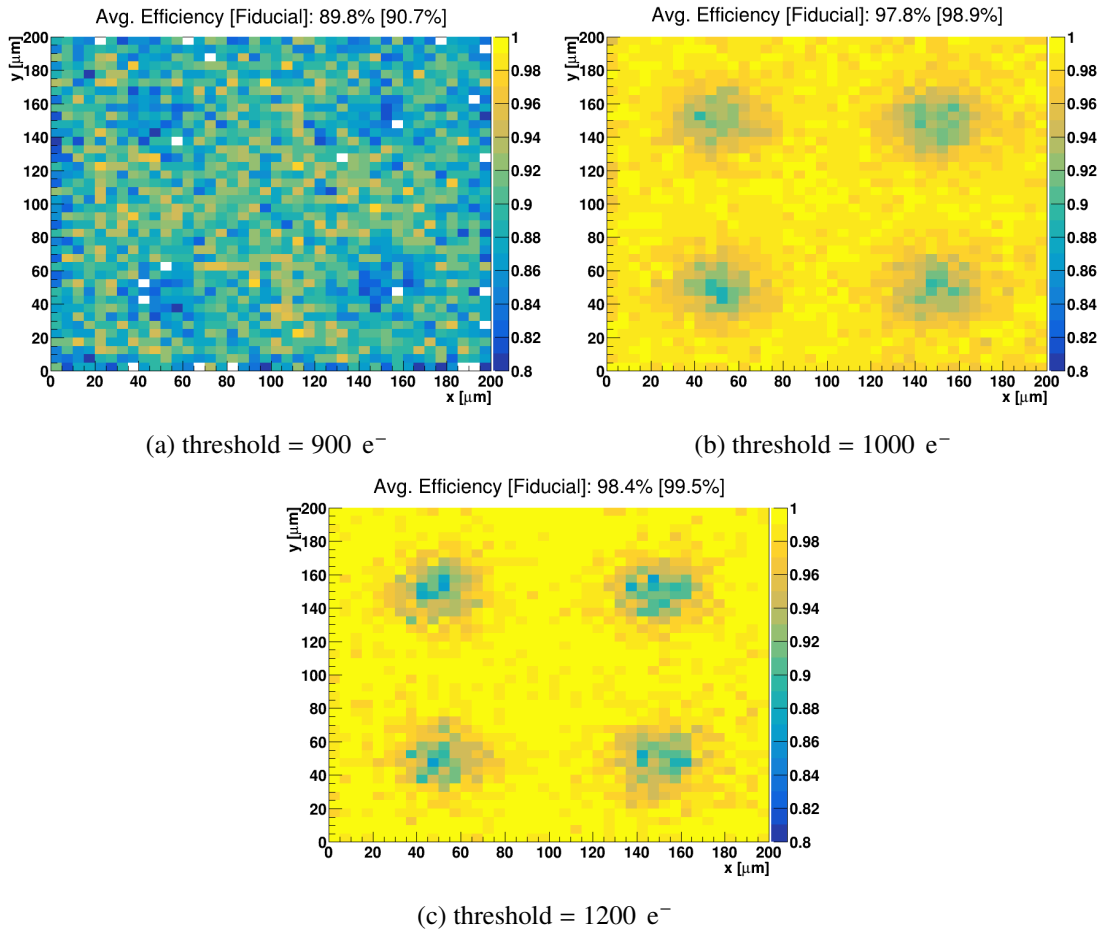


Figure 15: In-pixel efficiency maps, as defined in Section 4.2, for device DUT-B (linear FE) with $V_{\text{bias}} = 600 \text{ V}$

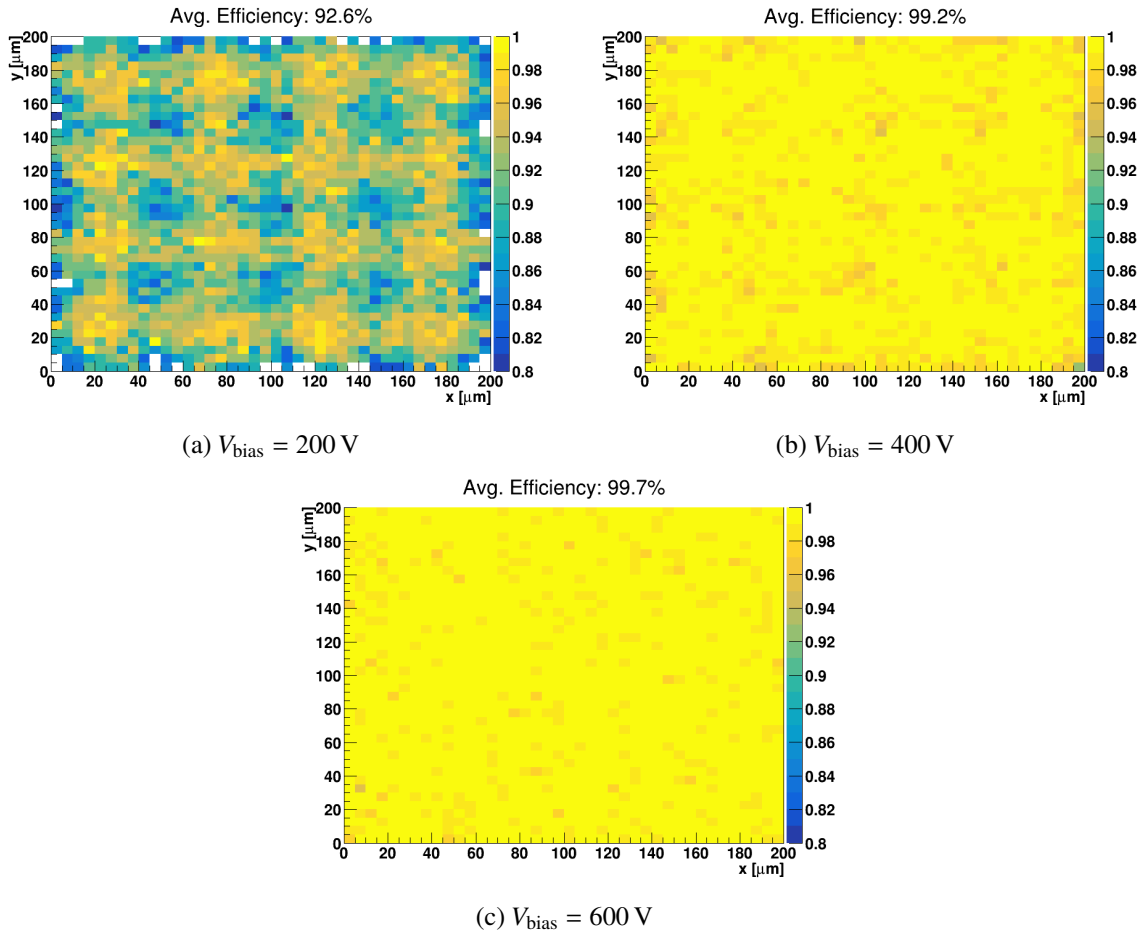


Figure 16: In-pixel efficiency maps, as defined in Section 4.2, for device DUT-A (linear FE) with threshold = 1027 e^- .

5.3 Cross-testbeam comparisons

Comparisons are performed between the October 2018 and December 2018 testbeams where the same devices were tested during both campaigns. Where overlapping operating parameters are present, bias and threshold scans are combined and summarised.

Figure 17 shows the overall efficiency as a function of the threshold for all devices under test at both October and December testbeam campaigns, selecting runs with $V_{\text{bias}} = 600 \text{ V}$. The efficiency generally increases when increasing the threshold to above 1000 e^- , at which point the effect of noise is reduced. Once the threshold reaches an optimal working point, efficiency will decrease as the threshold is increased further, as signal loss begins to occur. For all devices under test, the desired 97% efficiency is surpassed for optimal operation thresholds.

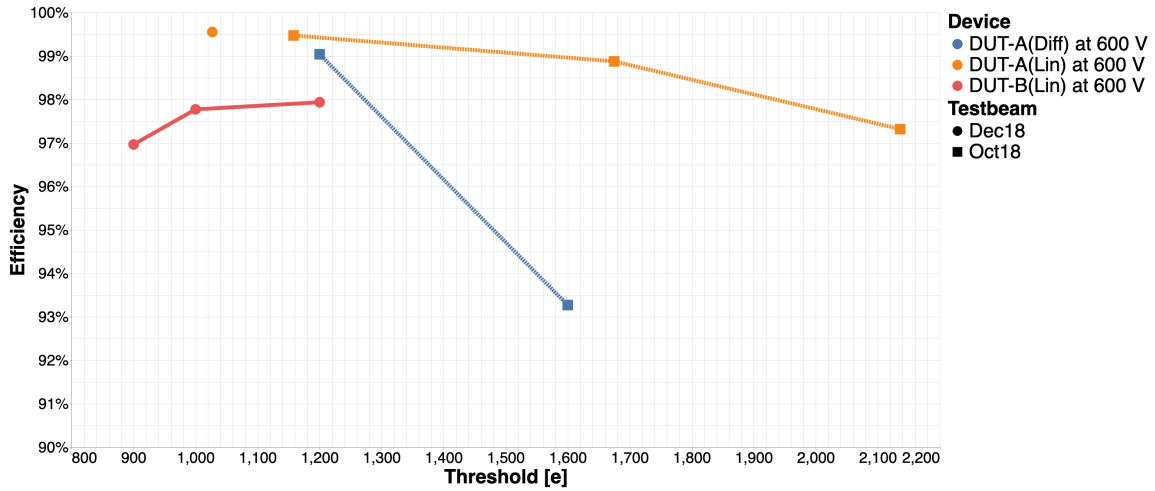


Figure 17: Overall pixel efficiency as a function of threshold for both October and December testbeam campaigns, selecting runs with $V_{\text{bias}} = 600 \text{ V}$.

Figure 18 shows the overall efficiency as a function of V_{bias} for both testbeam campaigns, selecting runs with FE threshold of $\text{th} = 1200 \text{ e}^-$. As discussed in Section 5.2, a turn-on curve is observed for device DUT-B (lin). The required efficiency is observed for all devices with $V_{\text{bias}} \geq 400 \text{ V}$.

6 Conclusions

Hybrid pixel detectors consisting of a planar silicon sensor bump-bonded to an RD53A readout chip have been characterised by the analysis of reconstructed testbeam data. Measurements were made using an EUDET-like beam telescope over two testbeam campaigns at the CERN SPS and DESY testbeam facilities in October 2018 and December 2018, respectively. Two devices were measured, with and without punch-through biasing structures, and using both linear and differential readout modes. Both devices used sensors with pixel pitch $50 \times 50 \mu\text{m}^2$, thickness of $150 \mu\text{m}$ and irradiated to $3.4 \times 10^{15} \text{ n}_{\text{eq}} \text{ cm}^{-2}$.

A range of V_{bias} and threshold scans were performed on the devices, with each device required to surpass 97% efficiency at $V_{\text{bias}} = 400 \text{ V}$.

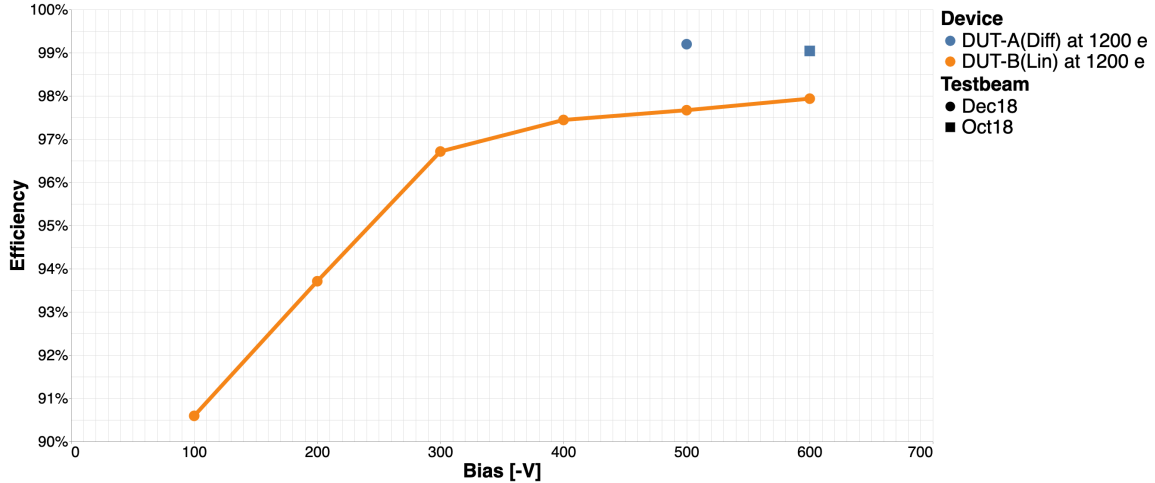


Figure 18: Overall efficiency as a function of V_{bias} comparing data from both testbeam campaigns, selecting the runs with FE threshold of $th = 1200 e^-$.

Across devices, the efficiency is observed to increase as the V_{bias} or threshold is increased until reaching an efficiency plateau. When the threshold is increased further, it is seen to reduce the device efficiency as signal hits begin to be cut away.

Devices which feature a punch-through bias structure are seen to reach an efficiency plateau at lower V_{bias} and threshold than those with no such structure. The efficiency at the plateau is also observed to be lower than the device with no biasing structure. In-pixel efficiency maps show regions of low efficiency around the punch-through dots on the device with the biasing structure.

At $V_{\text{bias}} = 600 \text{ V}$, the highest global efficiency was observed on device DUT-A, using the linear front-end with no punch-through biasing structure, at 99.6% efficiency, at a threshold of $threshold = 1158 e^-$. At the same V_{bias} , threshold, and operating mode, device DUT-B with a punch-through bias structure was observed to have a global efficiency of 98.4% and an efficiency of 99.5% in the fiducial area which masks out the regions contaminated by the biasing structure.

Although the biasing structure is seen to have a detrimental effect on the efficiency of the sensor, devices both with and without this feature comfortably surpass the 97% efficiency criteria. As such, the benefits provided by these biasing structures for production of modules is considered to outweigh the slight drop in efficiency which does not impact the ability of the device to pass QC criteria.

Device DUT-A was observed to achieve greater efficiency using the linear front-end than when using the differential front-end. At $V_{\text{bias}} = 600 \text{ V}$ and a threshold of around $1200 e^-$, the linear front-end produced a global efficiency of 99.6% whilst the differential front-end produced a global efficiency of 99.2%. In addition to this, the efficiency of the differential front-end was observed to fall off more quickly as the threshold was raised. At $V_{\text{bias}} = 600 \text{ V}$ and a threshold of around $1600 e^-$, the linear front-end produced a global efficiency of 98.9% whilst the differential front-end produced a global efficiency of 93.6%. In the absence of thresholds below around $1200 e^-$ to make comparisons with, and given that the differential front-end is expected to be capable of operating at lower threshold than the linear front-end, it is possible that the efficiency of the differential front-end

simply peaks at lower threshold than the linear front-end and could therefore outperform the linear front-end at these lower thresholds. Additional data points at these lower thresholds would be required to verify this.

Acknowledgments

The measurements leading to these results were made at the testbeam facility at DESY Hamburg (Germany), a member of the Helmholtz Association (HGF). We gratefully thank the operators of this facility.

The reconstruction and analysis presented here was performed within a framework based on one originally developed in collaboration with Tobias Fitschen. Our thanks to him for this.

References

- [1] A. Macchiolo, *The Phase-2 ATLAS ITk pixel upgrade*, *Nuclear Instruments and Methods in Physics Research Section A: Accelerators, Spectrometers, Detectors and Associated Equipment* **962** (2020) 162261.
- [2] J. S. Keller, *The ATLAS ITk strip detector system for the High Luminosity LHC upgrade*, *Nuclear Instruments and Methods in Physics Research Section A: Accelerators, Spectrometers, Detectors and Associated Equipment* **958** (2020) 162053.
- [3] S. Möbius, *Module development for the ATLAS ITk pixel detector*, *Journal of Instrumentation* **17** (2022) C03042.
- [4] RD53 COLLABORATION collaboration, *The RD53A Integrated Circuit*, tech. rep., CERN, Geneva, Oct, 2017. <https://cds.cern.ch/record/2287593>.
- [5] Karlsruhe Institute of Technology, “KIT Proton Irradiation.” <https://www.etp.kit.edu/english/264.php>.
- [6] ATLAS Collaboration, *ATLAS Inner Tracker Pixel Detector: Technical Design Report*, tech. rep., 2017. <https://cds.cern.ch/record/2285585>.
- [7] J. Wenninger, “SPS operation.” <https://jwenning.web.cern.ch/SPS.html>.
- [8] H. Jansen et al., *Performance of the EUDET-type beam telescopes*, *EPJ Tech. Instrum.* **3** (2016) 7 [1603.09669].
- [9] M. Daas, Y. Dieter, J. Dingfelder, M. Frohne, G. Giakoustidis, T. Hemperek et al., *BDAQ53, a versatile pixel detector readout and test system for the ATLAS and CMS HL-LHC upgrades*, *Nuclear Instruments and Methods in Physics Research Section A: Accelerators, Spectrometers, Detectors and Associated Equipment* **986** (2021) 164721.
- [10] DESY, “Generation of the desy test beams.” https://particle-physics.desy.de/test_beams_at_desy/e252106/e252211.
- [11] A. Himmi et al., *Mimosa26 User Manual*, tech. rep., December, 2008. https://www-rnc.lbl.gov/hft/hardware/docs/Phase1/M26_UserManual.pdf.
- [12] RD53 collaboration, *The RD53A Integrated Circuit*, tech. rep., CERN, Geneva, Oct, 2017. <https://cds.cern.ch/record/2287593>.
- [13] M. Garcia-Sciveres et al., *The FE-I4 pixel readout integrated circuit*, *Nucl. Instrum. Meth. A* **636** (2011) S155.
- [14] P. Baesso, D. Cussans and J. Goldstein, *The AIDA-2020 TLU: a flexible trigger logic unit for test beam facilities*, *JINST* **14** (2019) P09019 [2005.00310].
- [15] T. Bisanz, H. Jansen, J.-H. Arling, A. Bulgheroni, J. Dreyling-Eschweiler, T. Eichhorn et al., *Eutelescope: A modular reconstruction framework for beam telescope data*, *Journal of Instrumentation* **15** (2020) P09020–P09020.
- [16] F. Gaede, T. Behnke, N. Graf and T. Johnson, *LCIO: A Persistency framework for linear collider simulation studies*, *eConf* **C0303241** (2003) TUKT001 [physics/0306114].
- [17] ilcSoft community, “GEometry API for Reconstruction.” https://ilcsoft.desy.de/portal/software_packages/gear/.

- [18] P. Ahlburg, S. Arfaoui, J.-H. Arling, H. Augustin, D. Barney, M. Benoit et al., *Eudaq—a data acquisition software framework for common beam telescopes*, *Journal of Instrumentation* **15** (2020) P01038–P01038.
- [19] C. Kleinwort, *General broken lines as advanced track fitting method*, *Nuclear Instruments and Methods in Physics Research Section A: Accelerators, Spectrometers, Detectors and Associated Equipment* **673** (2012) 107–110.
- [20] tbmon2 community, “TBmon2 - Testbeam Data Analysis Software.”
<https://gitlab.cern.ch/tbmon2/tbmon2>.